


Spontaneous parametric down-conversion in an organic DAST crystal

P. Moroshkin , A. Nagar, and Jimmy Xu

School of Engineering, Brown University, Providence, Rhode Island 02912, USA



(Received 9 April 2024; accepted 22 July 2024; published 21 August 2024)

Nonlinear optical effect of spontaneous parametric down-conversion (SPDC) is widely used to produce entangled photon pairs for quantum information research and applications. We report on SPDC in 4-N, N-dimethylamino-4'-N'-methyl-stilbazolium tosylate (DAST) crystals. While being an early-phase exploration, the experimentally measured yield of the down-converted photons at the optical telecom wavelength is already comparable to that in the state-of-the-art periodically poled potassium titanyl phosphate (KTP) crystal. It hints at a greater potential being available, especially in its crystal orientation with an order of magnitude higher nonlinear coefficient, which is unfortunately not accessible in the present setup. The findings make the DAST system a promising candidate for entangled photon sources at telecom wavelengths.

DOI: [10.1103/PhysRevA.110.023518](https://doi.org/10.1103/PhysRevA.110.023518)

I. INTRODUCTION

4-N, N-dimethylamino-4'-N'-methyl-stilbazolium tosylate (DAST) is an organic material, well known for its nonlinear optical properties and applications [1]. DAST is transparent for infrared radiation and is frequently used for the generation of tunable emission in the THz range via the nonlinear process of difference-frequency generation (DFG) [2–5]. DAST crystals possess extremely high second-order nonlinear optical susceptibility in the near-infrared range, $\chi^{(2)} \approx 10^3$ pm/V [6,7]. More recently, even higher optical nonlinearity was demonstrated in DAST microcrystals [8] and in thin DAST films grown and annealed on a glass substrate [9].

Besides DFG, other second-order nonlinear processes have been observed in DAST, such as second-harmonic generation (SHG) [6,8,9], optical rectification [7,10], and lasing [8]. Recently, we have proposed [11] that the spontaneous parametric down-conversion (SPDC) effect in DAST may be used to generate entangled photon pairs in a telecom band. In the SPDC process, a single pump photon is converted into two photons (idler and signal) at longer wavelengths, obeying the momentum and energy conservation. SPDC thus can be considered as an inverse process of SHG, for the degenerate signal and idler.

Optical parametric generation has been observed in organic crystalline materials, such as 2-amino-5-nitropyridinium-dihydrogen phosphate (2A5NPDP) [12]. An efficient phase-matched optical parametric amplification was also predicted in DAST [6] based on the experimental SHG data.

The high value of $\chi^{(2)}$ detected via SHG [6,8,9] makes DAST a perspective candidate for a high-yield source of entangled photon pairs for various applications in quantum communications using telecom fibers. In contrast to conventional inorganic nonlinear crystals, the efficiency of nonlinear processes in DAST can be tuned by applying external stress [11], thanks to its plasticity. Also typical of organics is its scalability and structural conformity, e.g., to a waveguide or a composite metamaterial [13]. One may expect that in a thin-film form, thinner than the effective coherence length

of SPDC, the phase-matching constraint could be alleviated. Here we present an experimental study of the feasibility of SPDC generation of entangled photons in a DAST crystal.

II. EXPERIMENT

A. Phase matching

In our experiments, DAST samples are illuminated with a linearly polarized emission of a cw semiconductor laser with a wavelength $\lambda_{\text{pump}} = 781$ nm. In order to maximize the expected SPDC yield, the phase-matching condition must be fulfilled in a crystal much thicker than the coherence length:

$$\frac{n_p}{\lambda_{\text{pump}}} = \frac{n_s}{\lambda_s} + \frac{n_i}{\lambda_i}, \quad (1)$$

where λ_s and λ_i are the wavelengths of the signal and idler, respectively, and n_p , n_s , n_i are the refractive indices of the material corresponding to the pump, signal, and the idler, respectively. It is assumed that the generated signal and idler beams are collinear with the pump. DAST is a monoclinic crystal, with the dielectric axes x_1 , x_2 , and x_3 almost parallel to the crystallographic axes a , b , and c , respectively. More precisely [1], x_2 is parallel to b , x_1 is tilted by the angle $\delta = 5.4^\circ$ with respect to a , and x_3 , by 3.2° with respect to c , as illustrated in Fig. 1(b). The corresponding three refractive indices of DAST: $n_1(\lambda)$, $n_2(\lambda)$, and $n_3(\lambda)$ have been reported in Refs. [1,14]. Moreover, the phase matching for the OPO in DAST at the telecom wavelengths has been analyzed and demonstrated experimentally in Ref. [6]. The same configuration is applicable to our experiment aiming at the detection of the SPDC in DAST.

The phase matching of type II can be obtained with the pump beam at $\lambda_{\text{pump}} = 781$ nm propagating in the (x_1, x_3) plane, at the angle θ with respect to the axis x_3 and polarized along the axis x_2 . In Fig. 2(a) we plot the wavelengths of both signal and idler, propagating collinear with the pump. The idler is polarized in the same direction as the pump, along the axis x_2 and the signal in the (x_1, x_3) plane. The degenerate SPDC with $\lambda_s = \lambda_i = 1562$ nm is obtained at $\theta = 46.9^\circ$.

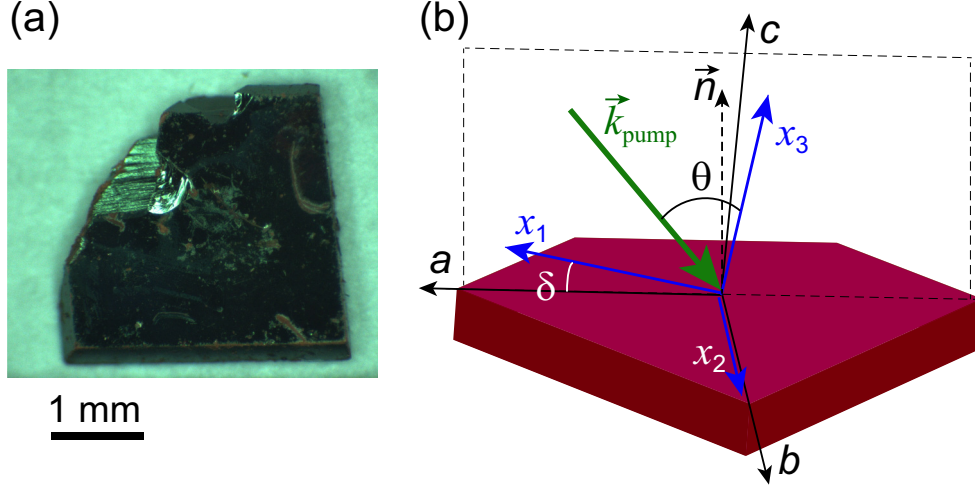


FIG. 1. (a) One of millimeter sized bulk DAST crystals used in the experiment. (b) A sketch of a DAST crystal, showing crystallographic axes (black solid arrows a , b , c), dielectric axes (blue solid arrows x_1 , x_2 , x_3), normal to the crystal surface (dashed black arrow \vec{n}), and the wave vector of the incident laser beam (green arrow \vec{k}_{Las}). A dashed rectangle shows the incidence plane.

When the plane of incidence is misaligned with respect to the (x_1, x_3) plane by the angle ϕ , the phase-matched signal and idler wavelengths change, as shown in Fig. 2(b). It is clear from Fig. 2 that the SPDC emission wavelengths much more strongly depend on θ than on ϕ . A small misalignment of the incident beam from $\theta = 46.9^\circ$ leads to large changes of λ_s and λ_i .

Unfortunately, due to the peculiarity of the crystal growth process in DAST, all DAST crystals available to us have the shape of a flat plate, with the large facets oriented parallel to the (a, b) plane. The desired propagation direction in the crystal and the normal to this surface form the angle $\psi_{1,2} = \theta \pm \delta = 51.3^\circ, 41.5^\circ$. With the refractive index $n_p = n_2(\lambda_{\text{pump}}) = 1.69$, both ψ_1 and ψ_2 are larger than the angle of total internal reflection at the DAST-air interface and thus cannot be achieved with the DAST crystal in the air. Therefore, in our experimental setup, the laser beam is coupled into the DAST crystal via a glass prism, as shown in Fig. 3.

B. DAST samples

In this study, we have used several DAST samples including bulk crystals provided by Rainbow Photonics and by colleagues in materials science, as well as thin-film crystals produced in our laboratory. The bulk crystals have a thickness $D \approx 0.1\text{--}0.4$ mm and a lateral dimensions of several millimeters. One such crystal is shown in Fig. 1(a).

The crystals grown by us were produced with the technique described in Ref. [15]. We use a methanol solution of DAST with the initial concentration of 40 g/l corresponding to the saturated solution at 45°C [16]. The crystals are grown in a $20\text{ }\mu\text{m}$ wide gap between two glass slides. The slides are inserted into the reservoir containing the DAST solution and the solution enters the gap under the action of the capillary force. The growth starts at the temperature of 45°C and proceeds with cooling the solution at a rate of 0.5°C per day, over 16 days. After that, the solvent is allowed to

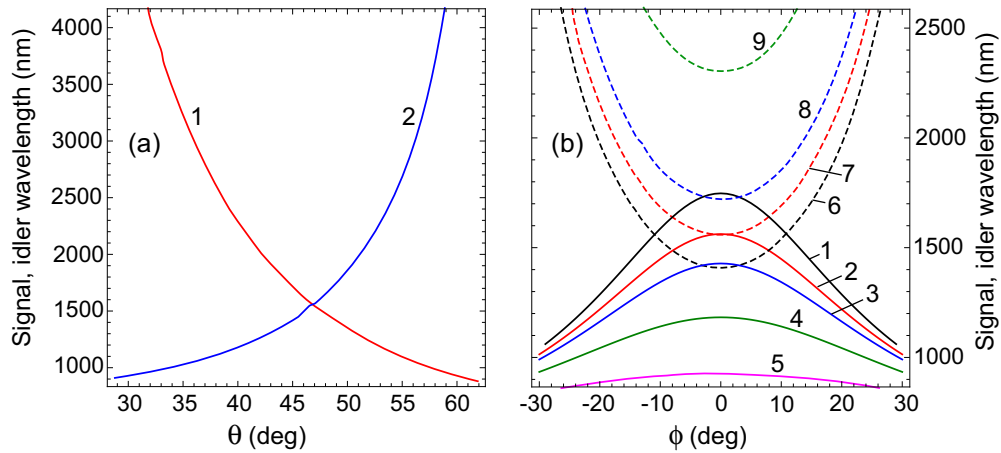


FIG. 2. Phase-matching curves for SPDC in DAST, type II, $\lambda_{\text{pump}} = 781$ nm. (a) Incidence in the (x_1, x_3) plane, pump polarized along x_2 . Signal (curve 1, red) and idler (curve 2, blue) wavelengths vs. the propagation angle θ . (b) The incidence plane rotated with respect to (x_1, x_3) by the angle ϕ . Signal (dashed lines) and idler (solid lines) wavelengths vs. ϕ . Curves 1, 6 (black): $\theta = 49^\circ$; curves 2, 7 (red): $\theta = 47^\circ$; curves 3, 8 (blue): $\theta = 45^\circ$; curves 4, 9 (green): $\theta = 40^\circ$; curve 5 (magenta): $\theta = 30^\circ$.

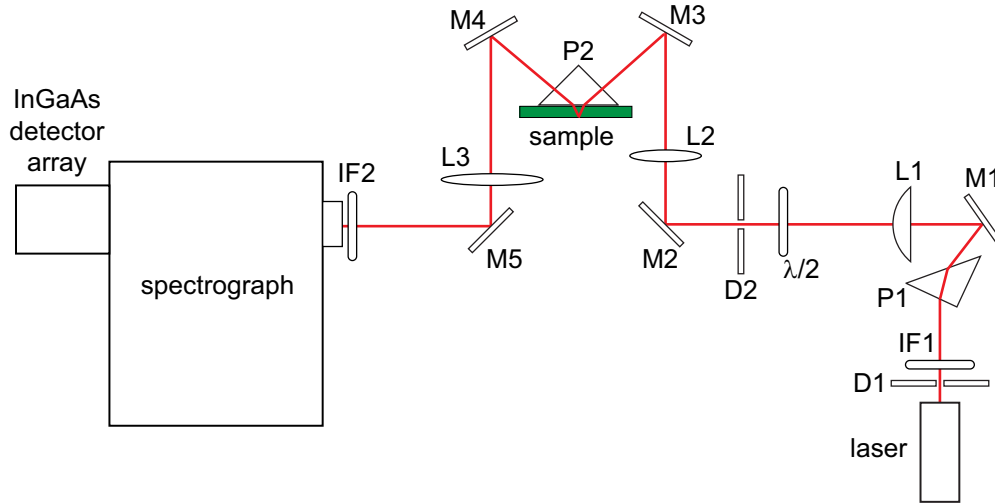


FIG. 3. Experimental setup. D1, D2: diaphragms; P1, P2: equilateral 90° prisms; L1–L3: lenses; M1–M5: mirrors; $\lambda/2$: half-wave plate; IF1 and IF2: short-pass and long-pass interference filters, respectively.

evaporate slowly over four days via the untightened lid of the container.

As a result, we obtain a large number of flat DAST crystals attached to either of the glass plates. The DAST plates have a thickness of several μm and a typical area in the range of $0.1\text{--}10\text{ mm}^2$. Despite the variety of shapes, one can clearly identify the edges with a 95° angle formed by (110) and (1–10) facets, hallmark of DAST crystals. We also observe the edges with the 132° angle corresponding to the intersection of the facets (110) and (010) [17]. These are indicative of DAST single crystals, in agreement with Refs. [15,16], with the large facets parallel to the (001) plane.

C. SPDC experimental setup

Our experimental setup for the observation of SPDC emission in DAST is shown in Fig. 3. The DAST sample is pumped by a cw semiconductor diode laser, $\lambda = 781\text{ nm}$, with the maximum output power of 1.6 W. Special care is taken to suppress the broadband amplified spontaneous emission emerging from the laser active medium together with the coherent laser beam. This infrared emission, although very weak, overlaps the spectral range of the SPDC and is sufficiently strong to overshadow the SPDC yield. As shown in Fig. 3, the output of the laser is passed through the prism (P1) and spatially filtered by two diaphragms (D1, D2) and a cylindric lens (L1). Additionally, the luminescence is suppressed by the short-pass interference filter (IF1). The spatial filtering reduces the astigmatism of the laser beam. The laser polarization is adjusted with the help of a half-wave plate.

The laser beam is focused with a $F = 150\text{ mm}$ lens (L2) to a spot $0.2 \times 0.3\text{ mm}$ (FWHM) onto the large facet of the DAST crystal. The beam enters the crystal via a 90° glass prism (P2) positioned on top of the crystal, in optical contact with the upper (001) facet. The contact is ensured by the index-matching liquid between the prism and the crystal. The beam then experiences a total internal reflection at the DAST-air interface at the lower facet and exits the crystal again via the upper facet and the prism. The light emerging from

the crystal is then focused onto the entrance slit of a grating spectrograph. The pump light reaching the spectrometer is blocked with a stack of long-pass interference filters (IF2), transmitting the emission at longer wavelengths. The signal of interest in the range of $900\text{--}1630\text{ nm}$ is detected with a 1D InGaAs photodetector array, mounted at the exit focal plane of the spectrograph.

III. RESULTS

A. Luminescence

Figure 4(a) shows a well-known emission spectrum of DAST crystals in the visible range. The spectrum was obtained from a millimeter-sized DAST crystal illuminated with a pulsed UV laser at $\lambda = 337\text{ nm}$. For comparison, we also show the emission spectrum of molecular DAST solution in methanol, under the same UV excitation. The spectra were recorded with a silicon CCD camera, sensitive in the range of $300\text{--}1000\text{ nm}$.

The visible emission spectrum of the DAST crystal is dominated by a strong band at $550\text{--}850\text{ nm}$ consisting of three partially overlapping peaks centered at 585, 626, and 720 nm. Similar spectra were reported by many [7,18–24]. The intensity ratios of the three peaks and their center wavelengths vary in different publications. Note that DAST is strongly absorbing in the wavelength range of $350\text{--}650\text{ nm}$ that partially overlaps with the emission band. The variations of the observed emission spectra thus can be attributed to the reabsorption of this emission in the crystal that depends on the crystal size and the spatial profile of the excitation laser beam.

In the following we concentrate on the near-infrared emission of DAST that was not reported in earlier works. A typical spectrum of the emission excited by the 781 nm laser is shown in Fig. 4(b). It is recorded with an InGaAs photodetector array sensitive in the wavelength range of $800\text{--}1700\text{ nm}$.

The main feature of the spectrum in Fig. 4(b) is peaked near 900 nm and its long-wavelength tail extends over the range of $900\text{--}1200\text{ nm}$. The abrupt cutoff at 900 nm is due to the long-pass interference filter that is used to suppress

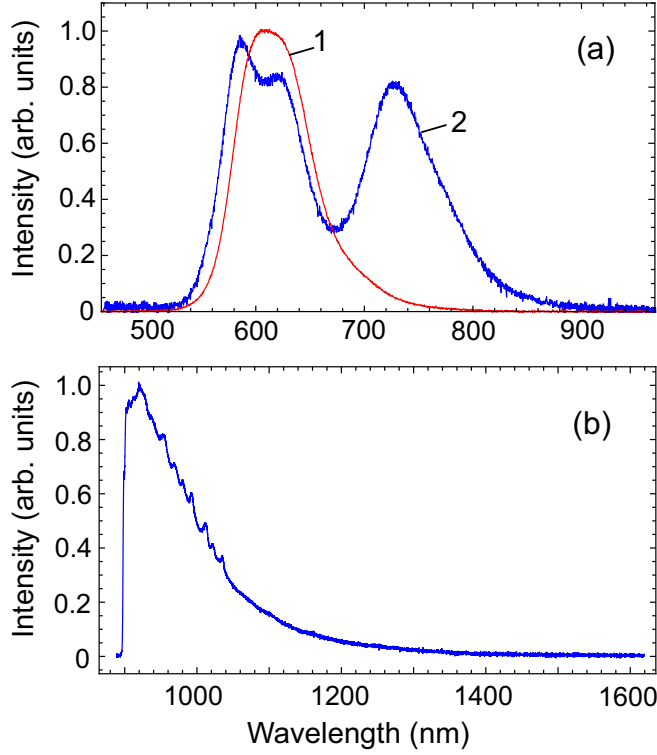


FIG. 4. (a) Emission spectra of DAST in the visible range. Red line: solution of DAST in methanol; blue line: DAST crystal. Excitation at 337 nm. (b) Near infrared emission spectrum of a DAST crystal. Excitation at 781 nm.

the scattered laser light at the entrance slit of the spectrometer. Unlike the SPDC emission being sought after here, the amplitude of this emission band only weakly depends on the incidence angle and polarization of the excitation laser light and on the direction at which light is collected. The shape of this band always remains the same. We therefore assign it to the long-wavelength part of the main luminescence band of DAST shown in Fig. 4(a).

B. Raman emission

In Fig. 4(b), on top of the main luminescence band at 900–1000 nm one can distinguish a group of eight narrow emission peaks. By repeating the same measurements with different laser wavelengths: $\lambda_{\text{Las}} = 808$ and 1064 nm, we have confirmed that this emission is due to the Raman scattering in the crystal. In Fig. 5(b) the same peaks are plotted vs. the Raman detuning, with the background luminescence spectrum subtracted. The same structure is observed under the excitation at $\lambda_{\text{Las}} = 781$, 808, and 1064 nm, shifting accordingly to the pump wavelength.

The Raman spectra of DAST have been reported and analyzed in Refs. [21,25]. However, all known Raman resonances are concentrated at lower frequencies, $\nu = 1000$ –1600 cm^{-1} . Figure 5(a) shows this part of the Raman spectrum that is also observed in our samples and is in a good agreement with the data of Refs. [21,25].

The new Raman band at $\nu = 2000$ –3200 cm^{-1} is observed in the bulk DAST crystals from two different providers and in

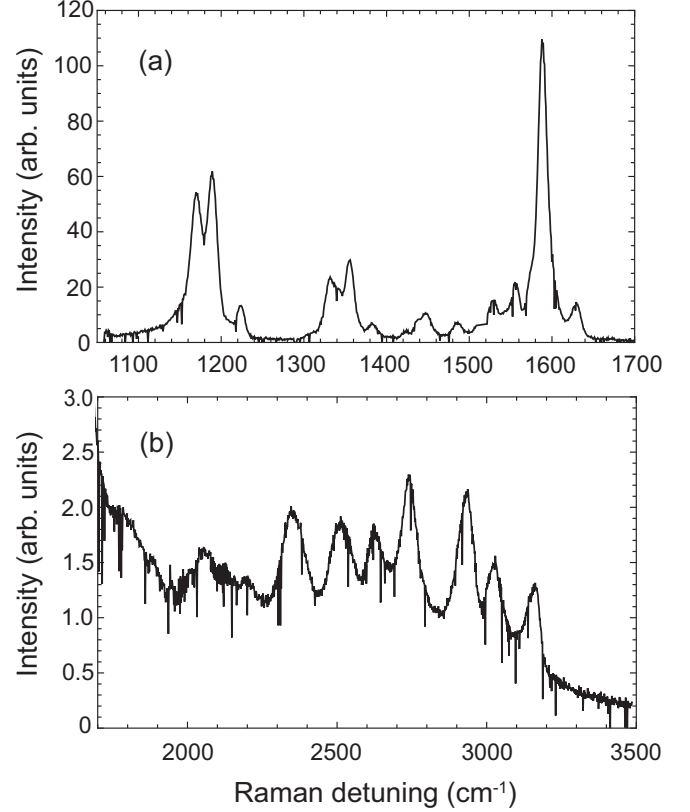


FIG. 5. Raman spectra of a bulk DAST crystal. (a) Spectral range of 1100–1700 cm^{-1} ; (b) spectral range of 1700–3500 cm^{-1} . The vertical scale in (b) is expanded by 40 times.

the thin DAST plates grown in our laboratory. It is therefore unlikely to originate from any impurity or contaminant. It was not observed in earlier studies, probably because of its low intensity. Under the same experimental conditions, it is approximately 50 times smaller in amplitude than the strongest Raman peak at 1577 cm^{-1} .

C. SPDC emission

The incident laser beam is set to propagate through the DAST crystal in the (x_1, x_3) plane, at the angle $\theta \approx 45^\circ$ – 50° with respect to the axis x_3 , to fulfill the phase-matching condition for a degenerate or near-degenerate SPDC process ($\lambda_s = \lambda_i = 1562$ nm at $\theta = 46.9^\circ$). As shown in Fig. 3, it is reflected at the lower surface of the crystal. Due to the angular mismatch $\delta = 5.4^\circ$ between x_3 and the normal to the crystal surface, after the internal reflection, this angle changes to $\theta' \approx 34^\circ$ – 39° . Under this condition, one expects a phase-matched nondegenerate SPDC with $\lambda'_s \approx 2240$ –3500 nm, $\lambda'_i \approx 1050$ –1200 nm.

Typical emission spectra obtained from a millimeter-sized bulk crystal pumped by a 500 mW laser beam are shown in Fig. 6. The SPDC emission appears on top of a strong laser-induced luminescence band discussed above in Sec. III A. In the spectra shown in Fig. 6, the luminescence spectrum is subtracted. The spectra are taken at the incidence angle of the laser beam that leads to $\theta \approx 49^\circ$ and $\theta' \approx 38^\circ$. The azimuthal angle ϕ is varied in steps of 1° from $\phi \approx 0$ to $\phi \approx 4^\circ$ by

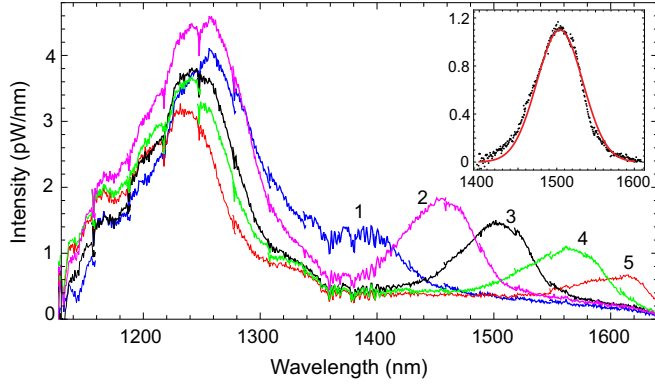


FIG. 6. DAST SPDC emission spectra. Excitation at 781 nm, $P_{\text{Las}} = 0.5$ W, type II phase matching. Fixed incidence angle ψ of the laser beam with respect to the crystal surface normal. Azimuthal angle ϕ varied in steps of 1° : curve 1 (blue): $\phi = \phi_0 \approx 0$; curve 2 (magenta): $\phi = \phi_0 + 1^\circ$; curve 3 (black): $\phi = \phi_0 + 2^\circ$; curve 4 (green): $\phi = \phi_0 + 3^\circ$; curve 5 (red): $\phi = \phi_0 + 4^\circ$. The inset shows an experimental SPDC spectrum (dots) at $\phi = \phi_0 + 2^\circ$ fitted with a Gaussian (solid line).

rotating the DAST crystal around the vertical axis. Under these conditions, within the spectral range of our detector, we observe two spectral components: the signal generated along the θ direction and the idler generated along θ' . The central wavelengths of both components vary with ϕ . The former shifts from 1400 nm to 1600 nm, the later, from 1260 nm to 1230 nm.

The experimental SPDC spectrum can be fitted with a Gaussian, as shown in the inset of Fig. 6. The FWHM spectral width of the SPDC peak near $\lambda = 1560$ nm typically varies in the range of 50–80 nm. It is quite comparable to the spectral width of SPDC generated in a periodically poled potassium titanyl phosphate (PPKTP) crystal pumped with a multimode laser diode [26], similar to the pumping laser used in our experiment. Small variations of the light collection angle in the vertical plane in the range of $\pm 0.2^\circ$, under a fixed incidence angle of the laser beam lead to the shift of the observed SPDC peak by 20–40 nm. We therefore conclude that the angular spread of the SPDC emission emerging from the DAST crystal exceeds the acceptance angle of our light collection system ($\Omega \approx 0.02$ strd) and that a part of this emission is generated under a noncollinear phase matching, resulting in a shifted emission spectrum.

According to Ref. [27], the total rate of SPDC emission into a single transverse mode is given by

$$R_T = \frac{(\chi^{(2)}\omega_p)^2 P_{\text{Las}} L}{3\pi^2 n_p n_s n_i \epsilon_0 c^2 W_p^2 (1 + \cos^2 \beta_i + \cos^2 \beta_s)} \times \frac{S}{n_i \cos \beta_i - n_s \cos \beta_s}, \quad (2)$$

where P_{Las} and W_p are the power and the Gaussian beam waist parameter of the laser beam, ω_p is the pump frequency, L is the effective crystal thickness, β_i and β_s , the angular mismatch of the idler and signal beams with respect to the pump, and S , a walk-off parameter. In the limit of collinear phase matching

and a small crystal thickness, it reduces to

$$R_T = \frac{(\chi^{(2)}\omega_p)^2 P_{\text{Las}} L}{9\pi n_p n_s n_i \epsilon_0 c^2 W_p^2 (n_i - n_s)}. \quad (3)$$

In our experimental setup, $P_{\text{Las}} \approx 0.5$ W, $W_p \approx 0.2$ mm, $n_p = 1.687$, $n_s = 1.772$, $n_i = 1.602$. The effective crystal thickness is $L = D / \cos(\theta + 5.4^\circ) \approx 0.6$ mm. Assuming collinear propagation of the pump, signal, and idler at $\theta \approx 47^\circ$, $\phi = 0$, the nonlinear susceptibility is given by $\chi^{(2)} = 2d_{\text{eff}} = 2(d_{212}\cos\theta + d_{232}\sin\theta)$. Here, d_{ijk} are the components of the susceptibility tensor. We use the experimental value of d_{eff} obtained in Ref. [6] by measuring second harmonic generation in the same experimental configuration: $d_{\text{eff}} \approx 12$ pm/V. The resulting expected SPDC yield in a single mode is $R_T \approx 1.7 \times 10^6$ photon pairs per second that corresponds to the conversion efficiency of 8.5×10^{-13} .

Experimentally, we typically obtain a spectrally integrated SPDC signal at a central wavelength near 1500 nm of the order of 20–160 pW, which corresponds to the photon count rate of $(1.5\text{--}12) \times 10^8 \text{ s}^{-1}$. The experimentally detected number of SPDC photons thus exceeds the theoretical prediction by more than 100 times. The actual number of emitted photons is even larger since some photons are lost before reaching the detector. The discrepancy arises, most likely, from the experimental geometry, with a large number of transverse modes contributing to the observed SPDC signal. The number of modes N_{tr} in each transversal direction can be estimated according to $N_{tr} = \sqrt{A\Omega}/\lambda$, where A is the area of the beam waist and Ω is its solid angular spread [28]. Assuming the SPDC beam waist area equal to that of the laser spot and the solid angle limited by the spectrometer acceptance angle, one obtains $N_{tr} \approx 30$ and the resulting total number of modes in both transversal directions is $N_{tr}^2 \approx 900$.

IV. DISCUSSION

The experimentally observed efficiency of a multimode SPDC emission in DAST in this work $\eta \approx (0.3\text{--}2.4) \times 10^6$ photons/s per 1 mW pumping power is quite comparable to and even exceeds the efficiency in the state-of-the-art PPKTP crystal, $\eta \approx 5.6 \times 10^5 \text{ s}^{-1} \text{ mW}^{-1}$ [26], although the latter is measured in a single spatial mode. The reported efficiency is still lower than that of a periodically poled LiNbO₃ waveguide, $\eta \approx 6 \times 10^7 \text{ s}^{-1} \text{ mW}^{-1}$ [29]. In the present experiment, some part of the generated infrared emission is produced by a noncollinear SPDC effect and is lost due to its broad angular spread. It is also worth noting that in the configuration dictated by the phase-matching conditions, one cannot access the largest component of the nonlinear susceptibility tensor, $d_{111} \approx 10^3$ pm/V [6], which otherwise could be used to raise the yield by another order of magnitude or two.

The SPDC yield can be increased by using thicker DAST crystals and by the optimization of the collection efficiency. Alternatively, it may be advantageous to use much thinner DAST films, for which the phase-matching condition is lifted, if the film thickness is smaller than the coherence length: $l_C = \lambda_{\text{pump}}/2(n_p - n_s) \approx 4.5 \mu\text{m}$. Recently, it was reported [9] that polycrystalline DAST films possess a greatly enhanced second-order nonlinearity, $\chi^{(2)} = 7.2$ nm/V, 300 times larger than the effective $\chi^{(2)}$ realized in the present work. The

enhancement is attributed [9] to a strain-induced increase in $\chi^{(2)}$, a very large effective surface area created by the recrystallized DAST films of densely packed microplates of crystallites, and alleviation of the phase-matching constraint. The $\sim 1/100$ decrease in the crystal thickness thus might be compensated by the increase in the nonlinear susceptibility and effective surface area.

V. CONCLUSIONS

In conclusion, we have demonstrated SPDC generation in DAST, an organic crystalline material with a large second-order nonlinearity. The experimentally measured yield of the multimode down-converted emission is significantly higher than expected on the basis of the effective second-order nonlinearity obtained in the literature [6]. The value is comparable to that of a classical inorganic counterpart, KTP. It may be

further improved by using either larger DAST crystals, or micrometer thick DAST films. Moreover, an order of magnitude or more is potentially available if the much larger d_{111} could be accessed in future explorations. Together, the results make DAST, as a representative system in the organic space, a promising candidate for novel entangled photon sources at the telecom wavelengths.

ACKNOWLEDGMENTS

This exploration was supported by ARO, Grants No. W911NF-21-1-0181 and No. W911NF-24-1-0138, by AFOSR, Grant No. FA 9550-19-1-0355, and by NASA EPSCoR program, Grant No. 23-2023 R3-0076 (B-001). We thank Xiandong Xu and Ruiliang Sun for supplying some of the DAST crystals we tested.

-
- [1] M. Jazbinsek, L. Mutter, and P. Günter, *IEEE J. Select. Topics Quant. Electron.* **14**, 1298 (2008).
 - [2] K. Kawase, M. Mizuno, S. Sohma, H. Takahashi, T. Taniuchi, Y. Urata, S. Wada, H. Tashiro, and H. Ito, *Opt. Lett.* **24**, 1065 (1999).
 - [3] J. Liu and F. Merkt, *Appl. Phys. Lett.* **93**, 131105 (2008).
 - [4] T. Satoh, Y. Toya, S. Yamamoto, T. Shimura, K. Kuroda, Y. Takahashi, M. Yoshimura, Y. Mori, T. Sasaki, and S. Ashihara, *J. Opt. Soc. Am. B* **27**, 2507 (2010).
 - [5] Y. He, Y. Wang, D. Xu, M. Nie, C. Yan, L. Tang, J. Shi, J. Feng, D. Yan, H. Liu *et al.*, *Appl. Phys. B* **124**, 16 (2018).
 - [6] U. Meier, M. Bösch, C. Bosshard, F. Pan, and P. Günter, *J. Appl. Phys.* **83**, 3486 (1998).
 - [7] K. Takeya, T. Kamei, K. Kawase, and H. Uchida, *Opt. Lett.* **45**, 5348 (2020).
 - [8] T. Tian, Y. Wang, W. Zhang, B. Wang, C. Fan, G. You, S. Yuan, G. Xu, M. Li, C. Xu *et al.*, *ACS Photon.* **7**, 2132 (2020).
 - [9] X. Cheng, X. Xu, M. Zhang, Y. Jiang, Q. Wang, Y. Qiu, L. Zhou, T. Fan, and J. Xu, *ACS Appl. Nano Mater.* **5**, 3480 (2022).
 - [10] A. Schneider, M. Neis, M. Stillhart, B. Ruiz, R. U. A. Khan, and P. Günter, *J. Opt. Soc. Am. B* **23**, 1822 (2006).
 - [11] P. Moroshkin, A. Nagar, M. J. Yu, B. Cai, and J. Xu, in *2021 Conference on Lasers and Electro-Optics (CLEO)* (IEEE, Piscataway, NJ, 2021).
 - [12] I. D. W. Samuel, B. Villacampa, D. Josse, S. Khodja, and J. Zyss, *Appl. Phys. Lett.* **66**, 2019 (1995).
 - [13] K. Fan, X. Xu, Y. Gu, Z. Dai, X. Cheng, J. Zhou, Y. Jiang, T. Fan, and J. Xu, *ACS Photon.* **6**, 1674 (2019).
 - [14] F. Pan, G. Knöpfle, C. Bosshard, S. Follonier, R. Spreiter, M. S. Wong, and P. Günter, *Appl. Phys. Lett.* **69**, 13 (1996).
 - [15] O. D. Volpyan, I. Y. Denisyuk, Y. A. Obod, M. I. Fokina, Y. A. Ignateva, and E. B. Shekhanova, *Opt. Spectrosc.* **128**, 1870 (2020).
 - [16] B. Ruiz, M. Jazbinsek, and P. Günter, *Crystal Growth Design* **8**, 4173 (2008).
 - [17] T. Thomas, J. V. Ramaclus, F. P. Mena, E. Mosquera, P. Sagayaraj, and E. A. Michael, *Cryst. Eng. Comm.* **17**, 1989 (2015).
 - [18] A. K. Bhowmik, J. Xu, and M. Thakur, *Appl. Phys. Lett.* **75**, 3291 (1999).
 - [19] K. Kumar, R. N. Rai, and S. B. Rai, *Appl. Phys. B* **96**, 85 (2009).
 - [20] M. L. Zheng, K. Fujita, W. Q. Chen, X. M. Duan, and S. Kawata, *J. Phys. Chem. C* **115**, 8988 (2011).
 - [21] A. S. H. Hameed, C. Karthikeyan, S. A. Nisha, G. Louis, and G. Ravi, *Optik* **127**, 4011 (2016).
 - [22] K. Uda, Y. Tsuda, S. Okada, R. Yamakado, L. Sun, Y. Suzuri, M. S. White, M. Furis, P. Stadler, O. Dimitriev *et al.*, *ACS Omega* **4**, 4056 (2019).
 - [23] O. N. Bezkravnaya, G. N. Babenko, I. M. Pritula, A. D. Roshal, Y. A. Gurkalenko, A. A. Kozlovski, and E. I. Kostenyukova, *J. Non-Cryst. Solids* **535**, 119957 (2020).
 - [24] Y. Feng, X. Xu, J. Liu, J. Hu, K. Xiong, X. Cheng, M. Zhang, Y. Jiang, T. Fan, and J. Xu, *Opt. Mater.* **122**, 111795 (2021).
 - [25] C. Bosshard, R. Spreiter, L. Degiorgi, and P. Günter, *Phys. Rev. B* **66**, 205107 (2002).
 - [26] A. Lohrmann, C. Perumangatt, A. Villar, and A. Ling, *Appl. Phys. Lett.* **116**, 021101 (2020).
 - [27] A. Ling, A. Lamas-Linares, and C. Kurtz, *Phys. Rev. A* **77**, 043834 (2008).
 - [28] A. E. Siegman, *Lasers* (University Science Books, Sausalito, 1986).
 - [29] M. Bock, A. Lenhard, C. Chunnillall, and C. Becher, *Opt. Express* **24**, 23992 (2016).